JOURNAL OF SPACECRAFT AND ROCKETS
Vol. 44, No. 2, March–April 2007

Characteristics of a Central Bleed Jet in Supersonic Axisymmetric Base Flow

Joel P. Kuehner,* Blake B. Anderson,† and Jonathan G. Flittner†
Washington and Lee University, Lexington, Virginia 24450
and
J. Craig Dutton‡
University of Texas at Arlington, Arlington, Texas 76019

DOI: 10.2514/1.24838

The near-wake flow structure of a supersonic axisymmetric base flow with base bleed is investigated in detail using acetone planar laser-induced fluorescence. Global side-view and end-view images are analyzed to detect unstirred bleed fluid, which has been found to persist from the bleed orifice through reattachment (i.e., rear stagnation point). The characteristic size, shape, and location of the bleed fluid pockets are studied. This enables a comparison of the bleed jet structure for three different cases of mass flow rate of bleed fluid. In addition, the average location of the forward stagnation point and the primary and secondary recirculation regions are linked to the distributions of several statistics. The similarities and differences between two suboptimal bleed rate cases identify possible optimal locations for the central bleed jet to be directed. A stabilizing effect caused by increasing bleed rate is documented in many of the statistical quantities. Agreement between side-view and end-view image analysis confirms the ability of the processing technique to distinguish the unstirred bleed fluid in all images.

Nomenclature

A_b	=	base area
A_j	=	area of bleed jet fluid in side and end views
A_r	=	area of recirculation-region fluid in side and end views
c_j	=	centroid of bleed jet fluid area in end views
I	=	injection parameter
M_j	=	Mach number of bleed jet fluid
P_j	=	perimeter surrounding the area of bleed jet fluid in side views
R_b	=	base radius
Re_j	=	Reynolds number of bleed jet fluid
r	=	radial coordinate
$r_{j,\max}$	=	largest radial penetration of bleed jet fluid in side and end views
r_r	=	local recirculation-region fluid radius
$w_{j,\max}$	=	largest contiguous bleed fluid width in side views
x	=	axial coordinate
$x_{j,\max}$	=	largest axial penetration of bleed jet fluid in side views

Introduction

THE flowfield behind a supersonic blunt-base projectile, shown in Fig. 1, has been heavily investigated in the past to better understand the flow mechanisms that generate low pressure in the near wake [1]. This low-pressure region results in a considerable pressure or base drag on the projectile, which can amount to a significant portion of the total vehicle drag [2]. It has been well established that the entrainment of the free shear layer draws mass from the recirculation region, reducing the pressure on the blunt base [1]. The free shear layer forms when the afterbody boundary layer separates at the base corner through a series of expansion waves generating the border between the supersonic freestream and the recirculation region. The low-momentum, inner portion of the shear layer is returned toward the base, as it does not have enough momentum to pass through the recompression waves and associated adverse pressure gradient that form near the rear stagnation point. Because of the importance of the mixing physics in the shear layer, various afterbody modifications have been studied in an attempt to alter the shear layer structure and raise the base pressure. Techniques such as boattailing [3], applying subboundary layer disturbances [4,5], and injecting mass bleed into the base region [6] have been investigated. Although the first two methods alter the afterbody geometry alone, base bleed directs fluid into the near wake through the base surface to supply a portion of the entrainment needs of the shear layer, thereby increasing the base pressure. Raising the base pressure reduces the effects of base drag, which can have practical benefits such as increased projectile range or speed. It is the fluid dynamic mechanisms governing the mass injection process that are considered here.

The time-averaged base-bleed flowfield is shown schematically in Fig. 2 for three different mass flow rates of bleed fluid. The bleed rate is quantified using the nondimensional injection parameter I, which is equal to the mass flow rate of the bleed fluid divided by the freestream mass flux and the base area. The introduction of the bleed fluid alters the blunt-base flowfield seen in Fig. 1 depending on the value of the injection parameter and the entrainment requirements of the shear layer. When the bleed jet does not supply all of the entrainment needs (case A, Fig. 2), the primary recirculation region (PRR) comprises a large portion of the near wake. A secondary recirculation region (SRR) forms as an annulus around the bleed jet. As the bleed flow rate is increased, the forward stagnation point (FSP) leaves the base surface and moves downstream, marking the start of the PRR. The rear stagnation point (RSP) also moves downstream and indicates the end of the PRR. As the bleed rate increases, the SRR becomes comparable in size to the PRR (case B, Fig. 2). Once the bleed jet supplies more mass than the shear layer can entrain, the wake opens similar to a power-on condition (case C, Fig. 2). In this case, the SRR dominates the near wake, and the PRR no longer exists. As suggested by component models of the base-bleed process [6], the maximum base drag reduction (optimal bleed rate) occurs when the bleed jet supplies the amount of mass required

Received 27 April 2006; revision received 28 November 2006; accepted for publication 27 December 2006.

*Assistant Professor, Physics and Engineering Department. Member AIAA.
†Research Assistant, Physics and Engineering Department.
‡Professor and Chair, Mechanical and Aerospace Engineering Department, Box 19018. Associate Fellow AIAA.

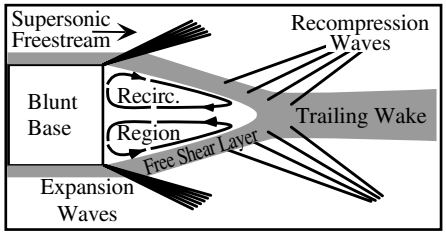

Fig. 1 Time-averaged supersonic blunt-base flowfield schematic.

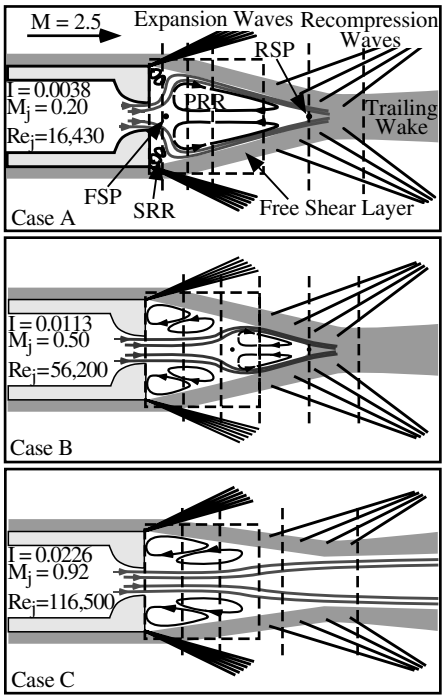

Fig. 2 Time-averaged base-bleed flowfield schematic and image locations. Dashed boxes indicate side-view image locations, and dashed lines indicate end-view locations. PRR—primary recirculation region; SRR—secondary recirculation region; FSP—forward stagnation point; RSP—rear stagnation point.

by the free shear layer entrainment, which occurs somewhere between cases B and C. This has been previously determined using base pressure measurements to be $I = 0.0148$ for the afterbody and flow conditions used in this study [7].

Although the injection parameter value can be correlated to base drag reduction, there is evidence that the size [6,8–10], number [8,11], position [12], and shape of the bleed orifices [6,9], as well as the momentum [13] of the bleed fluid, should also be considered. However, aside from several early studies, there has been little examination of these bleed orifice effects. This is mostly due to the cost involved in manufacturing and operating such a facility. This lack of investigation is still surprising, however, given the nonintrusive techniques that have been developed recently which could better investigate these flows. These exact concerns were raised by Zakkay and Sinha in their 1969 report [11]: "... these experiments ... must be continued and possibly even refined .... Extensive experimental data in far and near wake including the base region is needed before a full understanding of the problem is achieved .... Detailed studies of the near and far wake regions with base injection under different schemes are required before a full assessment of the various injection techniques can be made."

Recently, two planar laser-induced fluorescence (PLIF) imaging studies provided insight into the instantaneous flowfield behavior of a supersonic base flow with mass bleed [14,15]. These investigations seeded the bleed fluid with acetone, thereby allowing the near-wake flow structure to be investigated. In both studies, the images demonstrated that the instantaneous flowfield varied greatly from the anticipated time-mean flow features sketched in Fig. 2. Most importantly, large coherent regions of bleed fluid persisted from the bleed orifice into the trailing wake, remaining relatively unstirred (i.e., unmixed at large scales). Although the fluid motions in the recirculation region were expected to be relatively random based on previous laser Doppler velocimetry (LDV) results [7,16], these large, contiguous regions of unstirred bleed fluid pervading the near wake were not. Considering that base drag reductions are measured on a time-averaged basis using mean base pressure measurements, these rapid changes in bleed fluid structure afford the possibility that the base drag reduction also varies substantially with time about a mean value. This possibility agrees with recent findings for the blunt-base case (without bleed), for which the base pressure was found to fluctuate at high rates [17]. These base-pressure oscillations were also discovered to correlate with the instantaneous size of the recirculation region [18]. This link leads to the idea that there may be preferred forms of bleed fluid structure that increase base drag reduction, which are not only dependent on the value of the injection parameter but also on the effects of the central bleed jet on the near-wake flow structure. This concept was initially studied in a recent PLIF investigation [14] which demonstrated a similarity in flowfield features between the two suboptimal bleed rate cases investigated therein, cases A and B. Notably, the behavior just downstream of the SRR was similar for these two cases, although the mean downstream locations of these regions varied. With the difference in momentum of the two bleed streams for cases A and B, it is possible that the location and size of features like the SRR and the momentum with which the interactions occur assist in reducing base drag, and that the base bleed does more than simply supply an average amount of mass for the shear layer to entrain. Indeed, because it is the low-momentum portion of the shear layer that returns to the base, base drag reduction must be dependent on the magnitude and direction of the momentum flux of the bleed fluid.

This paper revisits the images of the previous PLIF work, focusing on the motions of the unstirred bleed fluid to investigate possible alternative mechanisms aside from the time-mean mass entrainment that affect base drag reduction. Statistical analysis will provide evidence of the locations where the bleed fluid exists in the near-wake region and will identify locations toward which the bleed stream could be directed such that optimal base drag conditions could be realized at lower bleed rates. This allows the results from the current afterbody to be used in directing future designs that should be investigated. Three bleed rates are considered, similar to the previous PLIF work, and are based on the measurements of Mathur and Dutton in the same facility [7]. Case A in Fig. 2 represents a very low, suboptimal bleed rate. Case B displays a slightly suboptimal condition. Finally, case C is postoptimal, representing an open-wake power-on condition.

Experimental Setup

Figure 3 displays a schematic of the supersonic, axisymmetric base-flow facility. Supersonic base flows with mass bleed have been investigated previously in this facility using LDV [7,16], Mie scattering [19], and PLIF [14,15], so a large database concerning the flowfield is available for comparison. In addition, several computational studies of the flowfield have been performed [20–22].

A detailed description of the experimental setup is provided in the previous PLIF report [14] and is reviewed briefly here. High-pressure air generates the supersonic freestream that passes over the afterbody

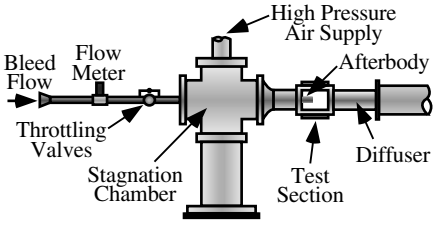

Fig. 3 Axisymmetric supersonic base-flow facility schematic.

Table 1 Axial coordinates of the end-view image locations, x/R_b, parallel to axis of symmetry

Case A	Case B	Case C
0.25	——	——
0.75	0.75	0.75
1.25	1.50	1.50
3.10	2.25	2.75
4.25	3.25	4.25
——	4.25	——

at a nominal Mach number of 2.5. The low-pressure condition in the near wake draws in room air through the forward-mounted sting, supplying the bleed fluid that is controlled by two valves in parallel and is measured using an electronic flow meter (Sierra 760). Before it enters the flow controller, the bleed fluid is seeded with vaporized acetone at a rate of 1% by mass. The afterbody has a diameter of 63.5 mm with a bleed orifice diameter of 25.4 mm. The bleed fluid passes through a converging nozzle before exiting the orifice.

A pulsed Nd:YAG laser (Continuum PL-8010) supplied the 266-nm light used to excite the acetone. The laser beam is formed into a sheet and passed through the test section. The resulting acetone fluorescence is captured with an intensified charge-coupled device (CCD) camera (Princeton Instruments PI-MAX-512-T). One global side-view image and multiple global end-view image locations were investigated for each case. The locations are marked in Fig. 2 by dotted lines. The global side-view image extends from the base to approximately 2.2 base radii downstream. The axial locations of the end-view images are given in Table 1. An ensemble of 600 images was acquired at each location. This ensemble size is slightly larger than used in similar Mie and PLIF studies of this flowfield and has been shown to provide statistically converged results [23]. Because of the spatial resolution of the images, the intensity represents a macroscopic stirring scale, rather than mixing at the molecular scale, hence the stirred/unstirred terminology used herein [14].

Image Processing

Sample instantaneous side-view and end-view images are presented in Figs. 4a and 4b, respectively. These images are from case A, and the end view was taken from location 1. These images display the distinct intensity levels that exist in all images in this study: the dark, unseeded freestream fluid, the gray, well-stirred recirculation-region fluid, and the bright, relatively unstirred bleed fluid. These levels are used to identify the different types of fluid present in the near wake. The recirculation-region fluid was found by thresholding each image at a level based on intensity histograms for the entire ensemble at a given location. The results of this process are shown in Figs. 4c and 4d.

The unstirred bleed fluid was found in a similar manner. For the side-view images, the location of the bleed orifice in the image is known and can be used to determine the unstirred bleed fluid intensity at the orifice exit. The average intensity over the first five columns outside the bleed orifice was employed in thresholding the image again. A correction of less than 10% was applied for the nonuniform laser sheet intensity found in the side-view images, both vertically and horizontally. Once the thresholding was completed, the image was further analyzed by retaining only the bleed fluid that is contiguous from the bleed orifice. The final set of pixels was despeckled using a 3×3 pixel window. The identified bleed fluid in the side-view image is shown in Fig. 4e.

Once the recirculation-region fluid was identified in the end-view images, the average recirculation-region intensity was found for each instantaneous image. The image was thresholded at 130% of this average value to locate the unstirred bleed fluid. The factor of 130% was determined by studying intensity histograms for the entire ensemble of end-view images. Because of the decrease in signal-to-noise ratio in the end-view images, the bleed fluid was despeckled using a 5×5 pixel window. A contiguity requirement, such as used in the side views, was not applied for the end views because no reference point exists and there is a general lack of cohesiveness of the bleed fluid in end-view images. The final result for the unstirred bleed fluid in the end-view image is shown in Fig. 4f.

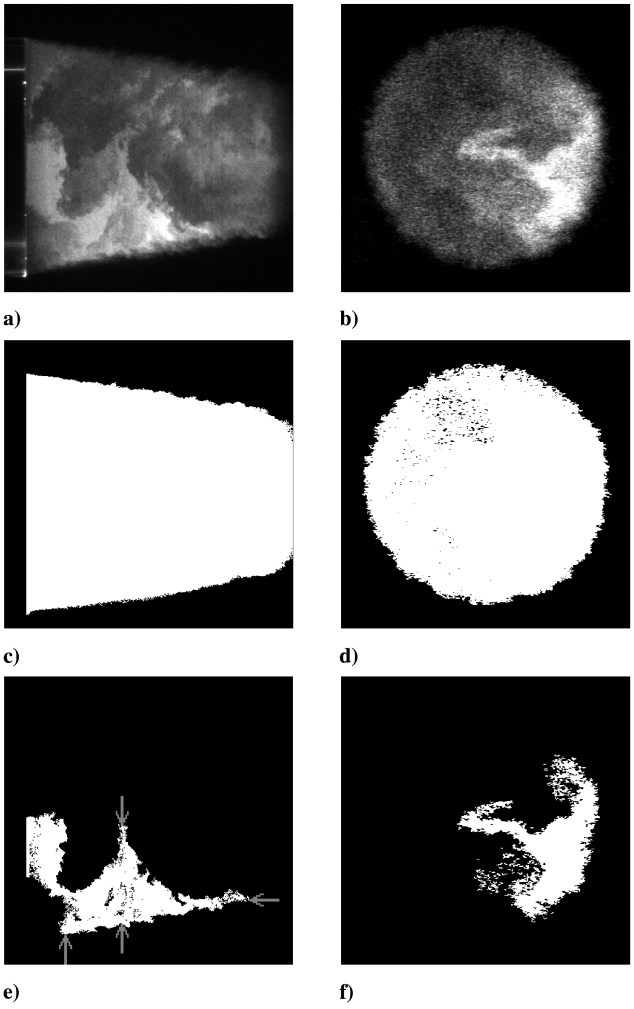

Fig. 4 Global side-view and end-view images from case A: a), b) original images; c), d) recirculation fluid; and e), f) bleed fluid.

It is important to restate the image locations before reviewing the results. The side-view images encompass the near-wake region over the approximate range of $x/R_b = 0$ to 2.2, where R_b is the base radius. The side-view images could not be enlarged to cover a larger downstream distance to maintain similar resolution between the side-view and end-view images. The end-view images represent the flowfield at unique downstream locations between $x/R_b = 0.25$ and 4.25, as given in Table 1. Therefore, comparisons of statistics from the side-view and end-view images must be done with care when referring to locations within the flowfield.

Flowfield Parameters

Once the bleed fluid and recirculation-region fluid are identified, a set of statistics is compiled for each ensemble. The initial thresholding procedure defines the recirculation-region fluid, which encompasses an area A_r. This is measured by the number of pixels passing the threshold criterion; see Figs. 4c and 4d. Similarly, the area contained within the bleed fluid, defined as A_j, can be calculated based on, for example, the number of pixels in Figs. 4e or 4f. Because A_j is a contiguous region in the side-view images, the length of the edge of the bleed fluid can be quantified and is referred to as the perimeter P_j.

For the side-view images, the largest axial, $x_{j,\max}$, and radial, $r_{j,\max}$, bleed fluid penetration locations are determined. Along with radial penetration, the maximum contiguous bleed fluid width, $w_{j,\max}$, from top to bottom of the image is found. This width does not

have to cross or be centered on the axis of symmetry. The quantities $r_{j,\max}$, $w_{j,\max}$, and $x_{j,\max}$ are identified from left to right by the gray arrows in the example side-view image of Fig. 4e. The downstream location of the maximum radial penetration and maximum width are also recorded. To investigate the bleed fluid orientation with respect to the flowfield centerline, the amount of bleed fluid above the centerline was determined. In the end-view images, A_r (Fig. 4d), A_j (Fig. 4f), and $r_{j,\max}$ can also be found. The centroid of the bleed fluid area is calculated, and its distance from the center of the average end-view image is defined as c_j.

To normalize the distances and areas determined from the images, the base radius R_b or base area A_b are often used. In addition to this, radial penetration and maximum width are normalized by the local recirculation-region radius r_r for each instantaneous image. In the side-view images, r_r is the distance between the axis of symmetry and the top of the recirculation-region fluid at the downstream location where the maximum width or radial penetration occurs. In the end-view images, r_r is determined by calculating the maximum distance between the center and the edge of the recirculation-region fluid for each image.

Results

Global Side-View Images

Figure 5 displays the histograms, or probability density functions, of the fraction of unstirred bleed fluid in the near wake on an instantaneous basis for all three bleed rates. Because the recirculation region size varies with the instantaneous amount of mass injected, the area of bleed fluid is normalized by the recirculation fluid area. On average, the fraction of unstirred bleed fluid increases from case A to C, which is expected from the increase in the injection parameter. The bimodal distribution in case A becomes more Gaussian in shape for case B. Looking at Fig. 5 for case C, the distribution narrows and the mean area ratio increases distinctly compared to that for the two lower bleed rates. This narrowing in distribution is in agreement with the increasing stability of the near-wake flow structure from cases A to C found in the previous study [14] and is seen in almost all statistics presented here. This stabilizing effect has also been encountered in other base-bleed studies [11,12].

The histograms for Fig. 5, cases A and B, reveal a most probable ratio (mode) of approximately 0.25 that has a similar distribution around the peak. The average area ratio is smaller in case A because of the second peak at an area ratio around 0.05. This indicates that for a large number of realizations, the amount of unstirred bleed fluid in the recirculation region is similar for cases A and B. This is one of several statistics that show similar characteristics, even though cases A and B provide different reductions in base drag and operate at different bleed rates. The difference in the histograms that occurs at average area ratios below 0.1 is due to the bleed jet retreating into the bleed orifice in case A, an effect that is never realized in case B. Other statistics are considered below to understand how the two cases compare.

Although the amount of unstirred bleed fluid increases on average with bleed rate, the average perimeter-to-area ratio of the bleed fluid decreases, as seen in Fig. 6. The uncertainty bars in this and all other plots represent 1 standard deviation in the ensemble of realizations about the mean. The perimeter-to-area ratio, which is related to the inverse of the fractal dimension, indicates how much of the fluid surface is available for mixing. The larger the ratio, the more potential for mixing there is. Figure 6 shows that as the amount of fluid injected increases from case A to C, the mixing potential decreases. This agrees with previous work, which found increased amounts of unstirred bleed fluid occurring at the start of the trailing wake as bleed rate increased [14].

To investigate whether this ratio is a good indicator of mixing potential, the maximum unstirred bleed fluid axial penetration distance is displayed in the histograms of Fig. 7. It is important to recall that the side-view images only extend downstream to

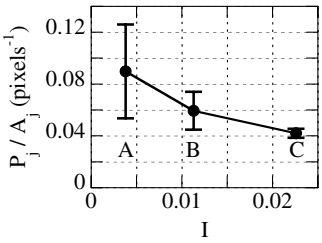

Fig. 6 Perimeter-to-area ratio of the bleed fluid for each case.

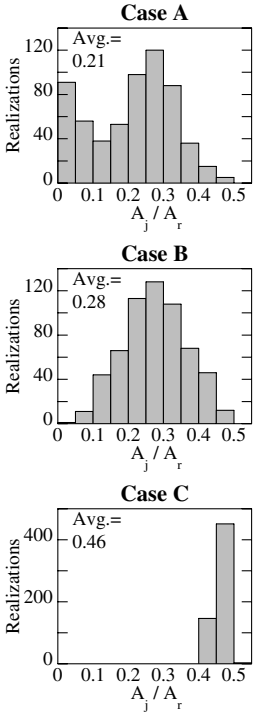

Fig. 5 Histograms of bleed fluid area normalized by recirculation fluid area for cases A–C.

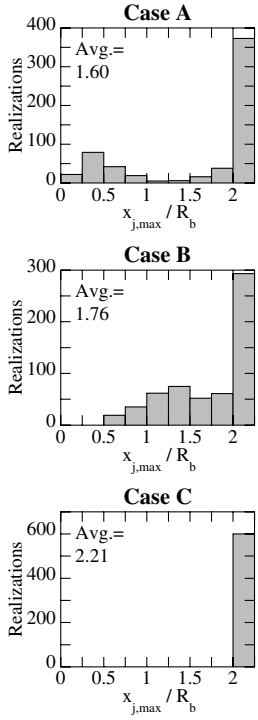

Fig. 7 Histograms of maximum axial penetration distance of the bleed fluid for cases A–C.

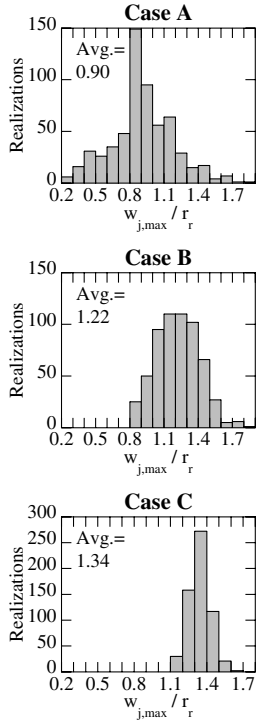

Fig. 8 Histograms of the normalized maximum bleed fluid width for cases A–C.

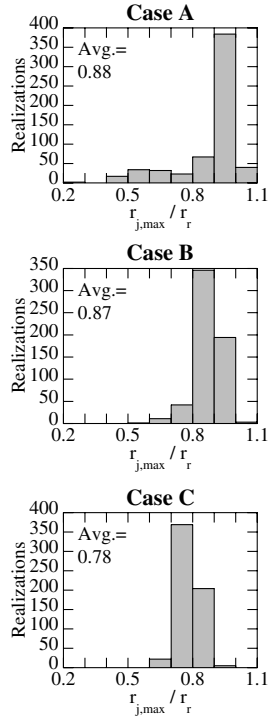

Fig. 9 Histograms of the normalized maximum radial bleed fluid penetration for cases A–C.

$x/R_b \sim 2.2$, so this represents the maximum value of this quantity that can exist for all cases. The average axial penetration of unstirred bleed fluid increases with bleed rate, which agrees with the likely reduction in mixing potential, P_j/A_j, that occurs with increasing bleed rate. There is a bimodal distribution of $x_{j,\max}/R_b$ for both cases A and B, where the location of bleed fluid penetration either occurs before the end of the image or beyond it. For case C, the unstirred bleed fluid always penetrates beyond the image location, as expected for the power-on condition. The stabilizing trend associated with increasing bleed rate appears again in the statistics for both Figs. 6 and 7. In addition, both statistics show a difference between cases A and B.

The increase in bleed fluid momentum and the decrease in mixing potential that is seen with increasing bleed rate helps to disperse the bleed fluid further downstream. However, it is also essential to identify where the bleed fluid exists radially in the near wake. The maximum width and the radial penetration of the bleed fluid are shown in Figs. 8 and 9, respectively. Because the PRR decreases in size from cases A to B, the maximum width increases. This can be explained with the streamline results from the LDV work [16], which display an increased space for the bleed fluid to exist in front (upstream) of the PRR. The smaller PRR and increased bleed fluid momentum for case B allows the bleed fluid to travel further downstream than for case A before being forced around the PRR. Additionally, as seen in the previous PLIF study [15], the bleed fluid in case A most often travels above or below the PRR, rather than around both sides simultaneously, therefore decreasing the maximum width that the bleed fluid attains. With the disappearance of the PRR and the increase in size of the SRR in case C, the bleed fluid has additional space to occupy and rather than being diverted by the effects of a PRR, it is only drawn to the shear layer by entrainment effects. Thus, the average maximum width increases for case C.

The opposite trend occurs for radial penetration, Fig. 9. As cases A and B both have a PRR, the fluid often gets ejected further from the axis of symmetry, whereas in case C bleed fluid is only pulled toward the shear layer by entrainment effects. Cases A and B display similar trends for this statistic even though the size of the PRR is different (see Fig. 2).

Analogous to axial penetration, the differences between cases A and B are highlighted when considering the average downstream locations of the maximum radial penetration and maximum width, as presented in Fig. 10. This implies that it might be the location of the unstirred bleed fluid, and not the specific amount, that is the difference between cases A and B. As expected, the axial location increases with increasing bleed rate for both statistics. This is most likely due to the downstream displacement of the FSP, the PRR, and the end of the SRR, all three of which should be related to the radial motion of the bleed fluid. The similarity between the average locations for maximum width and radial penetration of unstirred bleed fluid confirms that the physical mechanisms causing the two are similar. Based on the velocity measurements of Mathur and Dutton [16], the location of the FSP for case A ($x/R_b = 0.3$) and the locations of maximum width and radial penetration match well. However, the locations for both statistics for case B are approximately one base radius ahead of the FSP ($x/R_b = 1.8$), and one-half base radius before the end of the SRR ($x/R_b = 1.6$). For case C, the agreement between velocity and PLIF data returns, with the locations of the end of the SRR ($x/R_b = 2.0$), maximum width, and radial penetration agreeing closely. Case A displays the largest dispersion in location (see uncertainty bars in Fig. 10 representing 1 standard deviation about the mean), ranging from the bleed orifice to beyond the average start of the PRR.

There are two additional important differences between cases A and B. First, for all cases studied, the flowfield is axisymmetric on average; however, this is rarely true on an instantaneous basis for low bleed rates like case A. This is clearly evident in Fig. 11, which

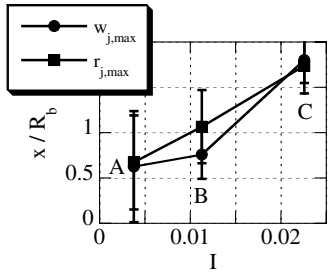

Fig. 10 Normalized axial location of maximum width and radial penetration for each side-view case.

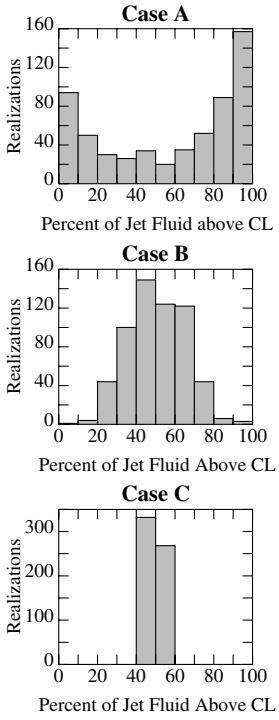

Fig. 11 Histograms of the percent of bleed jet fluid above centerline (CL) for cases A–C.

displays the percent of the bleed fluid above the centerline in each image. For case A, the condition encountered most often is for the bleed fluid to be almost completely above or below the axial centerline. This agrees with the finding in the previous PLIF study mentioned above [15]. This trend reverses for case B, where the distribution is more centered, but still substantially asymmetric for roughly half of the realizations. Case C is almost always centered, which again emphasizes the stabilizing nature of increasing the bleed rate. Based on these results, it might be useful to study orifice geometries that could force symmetry even at low bleed rates. One method for inducing symmetry would be to have numerous small orifices evenly spaced near the edge of the base with the flow directed toward the shear layer. The effects of the jets would be similar to those caused by the subboundary layer disturbances examined in the blunt-base no-bleed case, where delta-shaped tabs were affixed to the afterbody just upstream of the base corner [4]. These tabs generated streamwise vorticity that organized the random large-scale turbulent structures typically seen in the no-tab end-view images, thereby increasing the stability and symmetry of the free shear layer. Although this symmetry of the free shear layer does not ensure symmetry throughout the near-wake region, having the bleed fluid introduced near the free shear layer should aid in keeping the bleed fluid distribution symmetric. In addition, this style of injection has exhibited a further reduction in base drag over the style used in this study [8].

The second difference between cases A and B can be seen in Fig. 12. It was discovered in the LDV study that the velocity at the bleed orifice exit was axially downstream on average for all bleed rates. However, instantaneous velocity measurements indicated that bleed fluid retreated back into the bleed orifice on occasion [7]. This

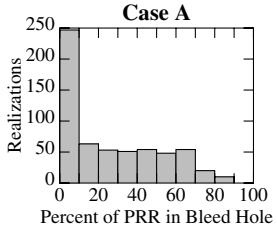

Fig. 12 Percent of bleed orifice exit inhabited by PRR fluid for case A.

was especially true for case A, for which the bleed fluid has little momentum on exit, and can be forced back into the bleed orifice by the motions of the PRR. Because the bleed fluid is identified at the orifice exit in the images, the number of pixels at the exit that are not marked as pure bleed fluid can be identified. These pixels are indicative of well-stirred PRR fluid being forced back into the bleed orifice. Figure 12 demonstrates this phenomenon with a histogram of the percentage of the bleed orifice that is composed of stirred PRR fluid. Histograms are not presented for cases B or C, because there were no realizations of this occurring in either ensemble, distinguishing low-momentum case A from the other two. Two important points can be made. First, over half of the ensemble has at least 10% of the bleed orifice taken up by PRR fluid (and not pure bleed fluid). Second, as the distribution is relatively flat beyond 10%, it appears that there is no preference for the amount of PRR fluid in the bleed orifice, which was not expected. While there is a slight drop for realizations over 70%, PRR fluid can often take up almost all or almost none of the bleed orifice. This reaffirms the low-momentum nature of the bleed fluid in case A and provides a reason for the large dispersion in most statistics for case A. However, there is no clear correlation between the existence of PRR fluid in the bleed orifice and any other statistic presented here. Therefore, no direct conclusion about the benefit or detriment of this occurrence can be made without further study.

Global End-View Images

Using the end-view images, the circumferential distribution of bleed fluid can be used as a comparison for the side-view statistics at specific downstream locations. Figure 13a displays the downstream dependence of the average bleed fluid area. Similar to the side-view statistics in Fig. 5, the peak value of A_j/A_r increases with bleed rate. Also comparable to the downstream distance of maximum width and radial penetration from the side-view images, shown in Fig. 10, the axial location of the peak value of A_j/A_r increases with increasing bleed rate. However, the peak value occurs approximately one base radius further downstream for cases B and C than is seen in the statistics from the side view. Even so, each case peaks near the end of the SRR or at the FSP and decreases after that point. Figure 13b also contains the dependence of the recirculation-region fluid area on downstream distance. These results agree very closely with the work of Bourdon and Dutton [19], who presented Mie scattering images of the outer freestream seeded with ethanol. In both investigations, A_r decreases almost identically for all three cases as the flow approaches reattachment.

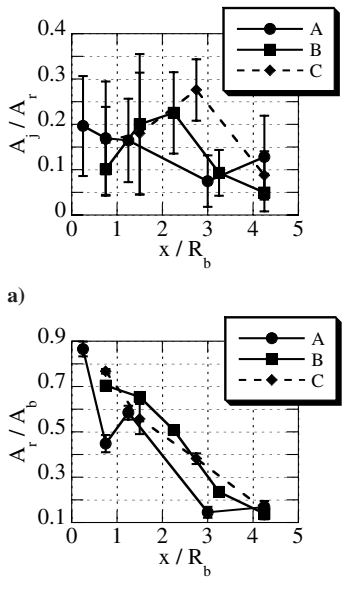

Fig. 13 a) Bleed fluid area normalized by recirculation fluid area and b) recirculation fluid area normalized by base area.

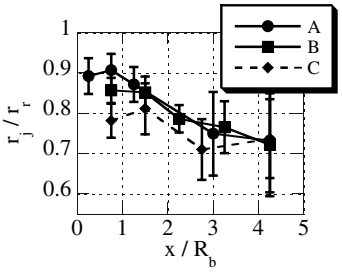

Fig. 14 Maximum radial bleed fluid penetration normalized by recirculation-region fluid penetration.

The downstream dependence of radial bleed fluid distribution can also be further investigated. Figure 14 displays the mean maximum radial fluid penetration from the center of the average end view. Similar to the side-view statistics of Fig. 9, the cases A and B statistics agree closely. Case C has a lower penetration distance on average, agreeing with the side-view images. The peak values of radial penetration occur at nearly the same positions in the end views as for the side views; see Fig. 10. This again indicates that the locations of the FSP and SRR are the controlling factors for the radial motion of the bleed fluid. The agreement between side-view and end-view image analyses verifies the capabilites of these procedures in identifying bleed and recirculation fluid in the images. All cases approach the same value with downstream distance. This is expected from Fig. 13b, because all of the flowfields approach the same recirculation-region area at this point. In addition, this matches the probability density functions of Kuehner and Dutton [14], which displayed similar mixing character at this downstream location. Somewhat unexpectedly, the dispersion in radial penetration data increases with downstream distance for all cases. For cases A and B, this could be explained by the disturbance caused by the PRR. In case C, the SRR ends at approximately $x/R_b = 1.5$, and the bleed fluid begins to directly interact with the shear layer. This interaction apparently causes the variability in the radial penetration data for this case.

The centroid of the bleed fluid can be determined in the end-view images, providing a comparable statistic to the percent of the bleed fluid above the centerline in the side-view images in Fig. 11. Rather than directly indicating a lack of axisymmetry, Fig. 15 indicates how much the bleed fluid moves as a bulk mass within the recirculation region. Early in the near wake, close to the FSP, the bleed fluid for case A is furthest from the center, and therefore attains the maximum centroid displacement from the centerline. The bleed fluid in case A is on average more than 30% of the distance to the edge of the base at this downstream location. Because the recirculation-region area is shrinking in size with downstream distance (see Fig. 13b), it is notable that the centroid can maintain a substantial distance from the centerline for the first three imaging locations in case A. This is relevant to the asymmetric distribution of bleed fluid seen in the side-view images for this case (Fig. 11). Midway along the PRR for case A, the bleed fluid becomes more contained, and the bleed fluid for case B becomes more outwardly distributed. For case B, the centroid distance peaks near the locations of the FSP and RSP, indicating the amount of fluctuation caused by these critical locations

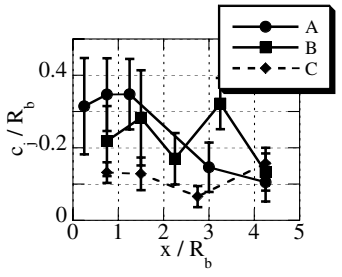

Fig. 15 Bleed fluid centroid distance from center normalized by base radius.

in the flow. The fact that case B is slightly more contained than case A in the upstream region is indicative of the axisymmetric tendency of case B over case A, as seen in Fig. 11. Case C demonstrates the most consistently small centroid displacement, again comparing well to the statistics of Fig. 11, although it is always away from the center by about 10% of the base radius on average. The centroid distance is minimized at the end of the SRR for case C, possibly indicating a stabilizing effect of the streamline expansion in this region.

Conclusions

Image analysis of a supersonic axisymmetric base flow with a central bleed jet illuminates the characteristics of the near-wake flowfield structure on an instantaneous basis. Several key points are found when studying the resulting statistics. First, there is a notable similarity between the two suboptimal bleed rates of cases A and B. It appears that the amount of bleed fluid occurring instantaneously within the near-wake flowfield varies greatly, and at times is quite similar for the two cases. However, the two cases can often be distinguished by the location of the bleed fluid in the near wake, especially at downstream positions. This provides the motivation to simultaneously obtain images of the bleed fluid structure along with high-speed base pressure measurements [18]. This would supply a possible link between the bleed fluid distribution and base pressure data studied here and previously.

Second, a distinct reduction in dispersion with increasing bleed rate is seen in almost all statistics. This is in agreement with the findings of the previous PLIF study [14]. However, it is in slight contrast to the velocity measurements, where the decrease in turbulence levels with increasing bleed rate reached a minimum for case B, rather than case C [16]. This reduction in flowfield unsteadiness indicates a stabilizing effect of increasing bleed flow rate, which should be monitored when searching for the optimal bleed orifice configuration.

Third, the bleed fluid remains relatively unstirred throughout most of the near wake and is distributed both radially and axially. This indicates that while the bleed fluid is eventually entrained into the shear layer and therefore reduces base drag, it also acts as a bulk mass that interacts strongly with the shear layer, the PRR, the SRR, and other instantaneous flow structures. This bulk motion must be considered when studying the benefits of base bleed and the design of future bleed orifice designs.

Acknowledgment

This research was funded through the U.S. Army Research Office under Grant DAAD19-01-1-0367 with Thomas L. Doligalski as Technical Monitor.

References

[1] Dutton, J. C., "Compressible Turbulent Free Shear Layers," AGARD, Rept. R-819, Neuilly-Sur-Seine, France, June 1997.

[2] Sahu, J., Nietubicz, C. J., and Steger, J. L., "Navier-Stokes Computations of Projectile Base Flow With and Without Mass Injection," *AIAA Journal*, Vol. 23, No. 9, 1985, pp. 1348–1355.

[3] Addy, A. L., and White, R. A., "Optimization of Drag Minimums Including Effects of Flow Separation," *Transactions of the ASME: Journal of Engineering for Industry*, Vol. 95, No. 1, 1973, pp. 360–364.

[4] Bourdon, C. J., and Dutton, J. C., "Mixing Enhancement in Compressible Base Flows via Generation of Streamwise Vorticity," *AIAA Journal*, Vol. 39, No. 8, 2001, pp. 1633–1635.

[5] Bourdon, C. J., and Dutton, J. C., "Altering Turbulence in Compressible Base Flow Using Axisymmetric Sub-Boundary-Layer Disturbances," *AIAA Journal*, Vol. 40, No. 11, 2002, pp. 2217–2224.

[6] Reid, J., and Hastings, R. C., "The Effect of a Central Jet on the Base Pressure of a Cylindrical After-body in a Supersonic Stream," Aeronautical Research Council (Great Britain) Reports and Memoranda No. 3224, Dec. 1959.

[7] Mathur, T., and Dutton, J. C., "Base-Bleed Experiments with a Cylindrical Afterbody in Supersonic Flow," *Journal of Spacecraft and Rockets*, Vol. 33, No. 1, 1996, pp. 30–37.

[8] Cortright, E. M., Jr., and Schroeder, A. H., "Preliminary Investigation of Effectiveness of Base Bleed in Reducing Drag of Blunt-Base Bodies in Supersonic Stream," National Advisory Committee for Aeronautics, TR RM E51A26, March 1951.

[9] Valentine, D. T., and Przirembel, C. E. G., "Turbulent Axisymmetric Near-Wake at Mach Four with Base Injection," *AIAA Journal*, Vol. 8, No. 12, 1970, pp. 2279–2280.

[10] Fu, J.-K., and Liang, S.-M., "Drag Reduction for Turbulent Flow Over a Projectile: Part I," *Journal of Spacecraft and Rockets*, Vol. 31, No. 1, 1994, pp. 85–92.

[11] Zakkay, V., and Sinha, R., "An Experimental Investigation of the Near Wake in an Axisymmetric Supersonic Flow With and Without Base Injection," *Israel Journal of Technology*, Vol. 7, No. 1–2, 1969, pp. 43–53.

[12] Badrinarayanan, M. A., "An Experimental Investigation of Base Flows at Supersonic Speeds," *Journal of the Royal Aeronautical Society*, Vol. 65, July 1961, pp. 475–482.

[13] Brazzel, C. E., and Henderson, J. H., "An Empirical Technique for Estimating Power-On Base Drag of Bodies-of-Revolution with a Single Jet Exhaust," *The Fluid Dynamic Aspects of Ballistics, NATO AGARD Conference Proceedings*, Mulhouse, France, Sept. 1966.

[14] Kuehner, J. P., and Dutton, J. C., "Planar Fluorescence Imaging of a Supersonic Axisymmetric Base Flow with Mass Bleed," *AIAA Journal*, Vol. 43, No. 8, 2005, pp. 1767–1775.

[15] Bourdon, C. J., and Dutton, J. C., "Visualization of a Central Bleed Jet in an Axisymmetric, Compressible Base Flow," *Physics of Fluids*, Vol. 15, No. 2, 2003, pp. 499–510.

[16] Mathur, T., and Dutton, J. C., "Velocity and Turbulence Measurements in a Supersonic Base Flow with Mass Bleed," *AIAA Journal*, Vol. 34, No. 6, 1996, pp. 1153–1159.

[17] Janssen, J. R., and Dutton, J. C., "Time-Series Analysis of Supersonic Base-Pressure Fluctuations," *AIAA Journal*, Vol. 42, No. 3, 2004, pp. 605–613.

[18] Cannon, P. M., Elliott, G. S., and Dutton, J. C., "Time-Series Axisymmetric Base-Pressure Measurements with Simultaneous Near-Wake Planar Visualizations," AIAA Paper 2005-5285, June 2005.

[19] Bourdon, C. J., and Dutton, J. C., "Turbulence Structure of a Compressible Base Flow with a Central Bleed Jet," *Journal of Spacecraft and Rockets*, Vol. 41, No. 3, 2004, pp. 451–460.

[20] Subbareddy, P., and Candler, G. V., "Numerical Investigations of Supersonic Base Flows Using DES," AIAA Paper 2005-0886, Jan. 2005.

[21] Subbareddy, P., and Candler, G. V., "Detached Eddy Simulation of Supersonic Base Flow with Bleed," AIAA Paper 2004-0066, Jan. 2004.

[22] Sahu, J., and Heavey, K. R., "Numerical Investigation of Supersonic Base Flow with Base Bleed," *Journal of Spacecraft and Rockets*, Vol. 34, No. 1, 1997, pp. 62–69.

[23] Smith, K. M., "The Role of Large Structures in Compressible Reattaching Shear Flows," Ph.D. Thesis, University of Illinois at Urbana–Champaign, Urbana, IL, 1996.

P. Weinacht
Associate Editor